Supporting Information for:

Investigating the Effect of Fe-N$_5$ Configuration in the Oxygen Reduction Reaction Using N-Heterocycle Functionalized Carbon Nanotubes

Qi Li,[a,b] Qi Zhao,[a] Angus Pedersen,[b,c] Mi Zhang,[a] Zhipeng Lin,[d] Yue Xu,[a,b] Patrick L. Cullen,[d] Andrei Sapelkin,[e] Devis Di Tommaso,[a,f] Maria-Magdalena Titirici,*[b] and Christopher R. Jones*[a]

a. Department of Chemistry, Queen Mary University of London, London, E1 4NS, UK.
b. Department of Chemical Engineering, Imperial College London, London, SW7 2AZ, UK.
c. Department of Materials, Royal School of Mines, Imperial College London, London, SW7 2AZ, UK.
d. School of Engineering and Materials Science, Queen Mary University of London, London E1 4NS, U.K.
e. Department of Physics, Queen Mary University of London, London, E1 4NS UK
f. Digital Environment Research Institute, Queen Mary University of London, Empire House, 67-75 New Road, London E1 1HH, UK

Experiment

Chemical and materials:

The chemicals and solvents mentioned in this paper were used without further purification unless otherwise stated. 4-Amino-pyridine, 5-amino-quinoline, 9-amino-acridine, 6-amino-isoquinoline, and isoamyl nitrite 98% (stabilized with potassium carbonate) were purchased from Fluorochem (UK) and the FePc from TCL (Tokyo Chemical Industry, UK). For the functionalization of carbon nanotubes, the CNTs (US 4403 Graphitized MWCNTs, 99.9% purity, OD 10-20 nm) were purchased from US Nano and used directly without further treatment. *ortho*-dichlorobenzene (*o*DCB) was purchased from Alfa Aesar (97%) and was dried over activated 4 Å molecular sieves, then purged with N$_2$ flow for at least 2 hours before use. The PTFE membrane filter was purchased from Sigma Aldrich (Ominipore, hydrophilic, 0.2 μm pore size). For the electrochemical test, ethanol (99.9%) was purchased from Sigma Aldrich (UK). Nafion D-521 (5wt.%, dispersed in water and 1-propanol) was purchased from Alfa Aesar. Suprapur Potassium hydroxide hydrate (Sigma Aldrich, 99.995%) was used to prepare the 0.1M KOH electrolyte. High-purity oxygen (≥99.9998% Ultrapure Plus, Air Products), nitrogen (≥99.99998% BIP Plus, Air Products), and hydrogen were used for electrochemical reference electrode calibration tests. Deionized water (18 MΩ·cm) was used for all experiments.

Characterization

The Ultraviolet-Visible Absorption Spectroscopy (UV-vis) was conducted on an Agilent Cary 100 UV-vis spectrometer. The morphology and structure of the samples were characterized using an FEI Inspect-F scanning electron microscope (SEM). For the sample preparation, about 1 mg in 1 mL absolute ethanol was bath sonicated for 10 min, then the drop 10 μL on a silicon wafer and left to dry in air overnight. TEM was performed on a JOEL 2100F. The TEM sample was prepared by sonicating 1 mg sample in 1 mL absolute ethanol for 10 min, then dropped on a copper TEM grid and left to dry in air overnight. XPS analysis was conducted employing a Thermo Fisher Nexsa X-ray Photoelectron Spectrometer system, and the high-resolution spectra were analyzed by the Avantage software with the FWHM of deconvoluted peaks set as equal for 1s spectrum. All spectra were calibrated relative to the carbon C 1s peak at 284.8 eV for correcting for charging effects. XRD patterns were obtained on an Xpert-Pro powder X-ray diffractometer with Ni-filtered Cu-Kα radiation (λ = 1.5418 Å) over the 2θ range from 5° to 120°, in steps of 0.0315°. Raman spectra were collected using a Renishaw inVia Raman microscope operated with an incident laser beam at 633 nm. The laser intensity was minimized to 0.5 mW to avoid heating the samples. CasaXPS software was used to deconvolute the peaks and to calculate the I$_D$/I$_G$ ratio. The line shape used in the fitting is GL(30) (Gaussian 30% and Lorentzian 70%). Inductively coupled plasma mass spectrometry (ICP-MS) was obtained using an Agilent 7900 spectrometer (Agilent Technologies). Before analysis, the CNT samples were carefully weighed and digested by aqua regia using a MARS 6 microwave at 1500 W for 20 min. The solutions were further filtered and diluted with 2% HNO$_3$ and 1% HCl to achieve a concentration of Fe < 500 ppb. The nitrogen sorption isotherms were conducted at −196 °C in a Quantachrome NOVA 4200e Surface Area & Pore Size Analyser system with about 15 mg of degassed sample (200 ℃ overnight). The pore size distribution was calculated by the DFT method from the adsorption isotherm on Quantachrome NOVAwin software.

X-ray Absorption (XAS) measurements were carried out at beamline B18 of the Diamond Light Source in Fluorescence mode. For XAS analysis, approximately 20 mg of sample were mixed with 10 mg cellulose and pressed into a 10 mm pellet with a thickness of 0.5 – 1 mm. The obtained data were normalized to the incident intensity and processed and analyzed using the Demeter

software package.[1] A linear function was subtracted from the pre-edge region, and then the edge jump was normalized using Athena software. A standard Fe foil was used to calibrate the beam energy and a derivative (E0) value of 7112.0 eV corresponding to the first inflection point of the absorption K-edge was obtained. XANES spectra were plotted after processing pre-edge and post-edge background and then normalizing to the edge step.

The XAS data were processed using Athena[1] and Spspline[2] for background subtraction to extract EXAFS spectra with subsequent analysis[1] performed using Artemis and FEFF codes[3]. Structural models used in the EXAFS fitting were built, and geometry optimized using VESTA (also applied for DFT calculation). The Fourier transformed EXAFS data of the catalyst materials is in the range of 3–10 Å^{-1} and 3–15 Å^{-1} for the other reference sample Fe, FePc, and FePcCl.

Computational details

Density functional theory (DFT) calculations were performed by the "Vienna ab initio simulation package" (VASP6.1.1).[4] We used the generalized gradient approximation (GGA) exchange-correlation functional proposed by Perdew–Burke–Ernzerhof (PBE),[5] together with the Grimme's-D3 dispersion correction.[6] Valence electrons were described by a plane wave basis set with an energy cutoff (Ecut) of 450 eV to optimize the intermediates and locate the intermediates and transition state structures on the reaction energy profile. Optimized intermediates were obtained by minimizing the forces on each ion until they were less than 0.05 eV/Å. Monkhorst-Pack k-point samplings of (3×3×1) were employed for optimized geometries and the intermediates' calculation. Monkhorst-Pack k-point samplings of (15×15×1) were employed for density of states (DOS) calculation and the projected density of states (PDOS) was processed by vaspkit.[7] The changes in the Gibbs free energy (ΔG) of each step were computed to determine the most favorable reaction pathway. For processes involving proton-electron transfer, the reaction energy was calculated using the computational hydrogen electrode method proposed by Nørskov and co-workers.[8] The free energy differences of the processes were computed according to the following expression:

$$\Delta G = \Delta E_{DFT} + \Delta E_{ZPE} - T\Delta S \tag{1}$$

Where ΔE_{DFT} is the total energy difference from the DFT calculations, ΔE_{ZPE} is the zero-point energy (ZPE) correction from the frequency analysis, and $T\Delta S$ is the entropy contribution at the temperature (T) of 0K. The limiting potential U_L is an important factor for evaluating the catalytic activity and is calculated by:

$$U_L = -\Delta G_{max}/ne \tag{2}$$

where ΔG_{max} is the relative change of the Gibbs free energy of the rate-determining step, n is the number of electrons transferred, and e is the electron charge. The overpotential (η) of the ORR on a catalyst is given by the difference between the equilibrium (Ueq, Ueq=1.23 V) and limiting potentials, which is described as the rate-limiting step[9]:

$$\eta = U_{eq} - U_L \tag{3}$$

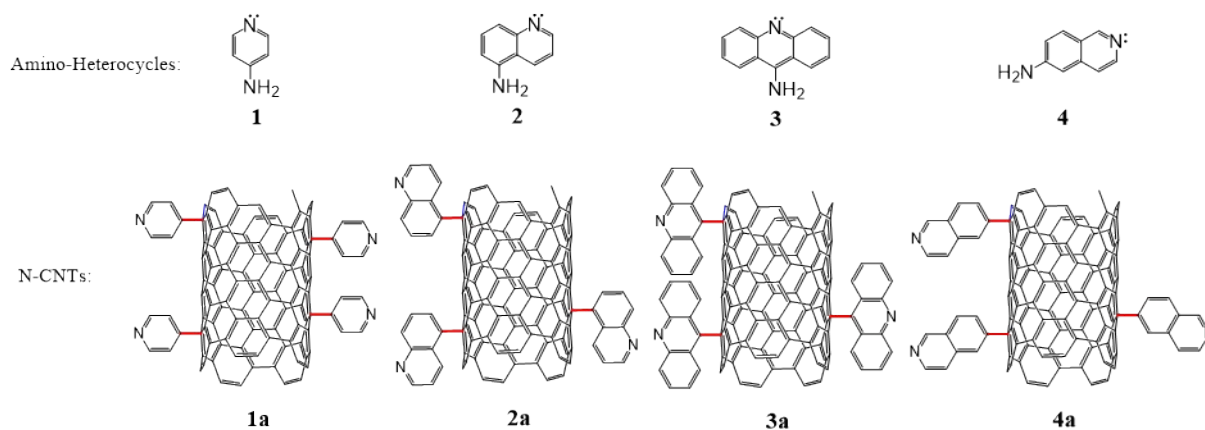Table S1 Preparation of *N*-heterocycle-functionalized CNTs.

Product	Precursor (mmol)	Reaction conditions			
		Isoamyl nitrite (mmol)	CNTs (mg)	Temperature (°C)	Time (h)
Py-CNT (1a)	4-amino pyridine (1.72)	3.44	40	100	24
Q-CNT (2a)	5-amino quinoline (1.72)	3.44	40	80	15
A-CNT (3a)	9-amino acridine (1.72)	3.44	40	80	15
IsoQ-CNT2 (4a)	6-amino isoquinoline (1.72)	3.44	40	80	15
IsoQ-CNT (4a)	6-amino isoquinoline (0.86)	1.72	40	80	15
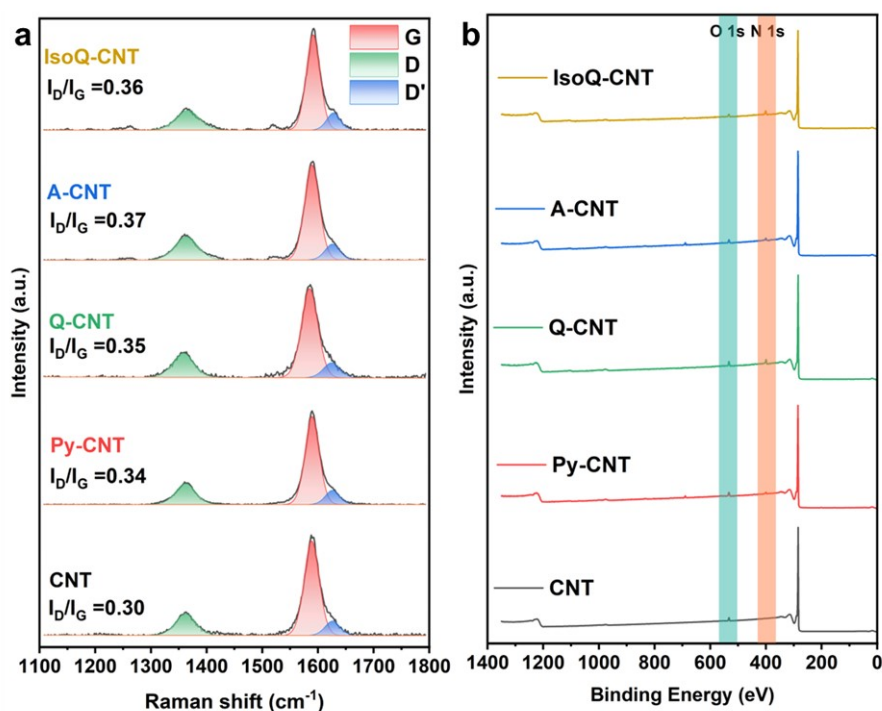
Figure S1 (a) Raman spectra and (b) XPS survey spectra of CNT, Py-CNT, Q-CNT, A-CNT, and IsoQ-CNT

Note 1: Three independent points were randomly tested in each sample and the average I_D/I_G was calculated based on them. Raman spectra were fitted with a peak for the D band (Green) at approximately 1360 cm^{-1}, a peak for the G band (Red) at approximately 1590 cm^{-1}, and a peak for the D' band at approximately 1620 cm^{-1} (blue). The full width at half maximum (FWHM) of the D band is approximately 40-45 and the FWHM of the D' band and G band is approximately 35. It has been reported that the calculated coherence length La of graphite significantly affected the potassium-ion battery's electrochemical performance.[10, 11] Here we further calculate the La of N-CNTs to provide a more quantitative description of the structure order along surface planes, based on the following equation according to the previous literature,[11, 12] and the *L*a of N-CNTs are shown in Table S2:

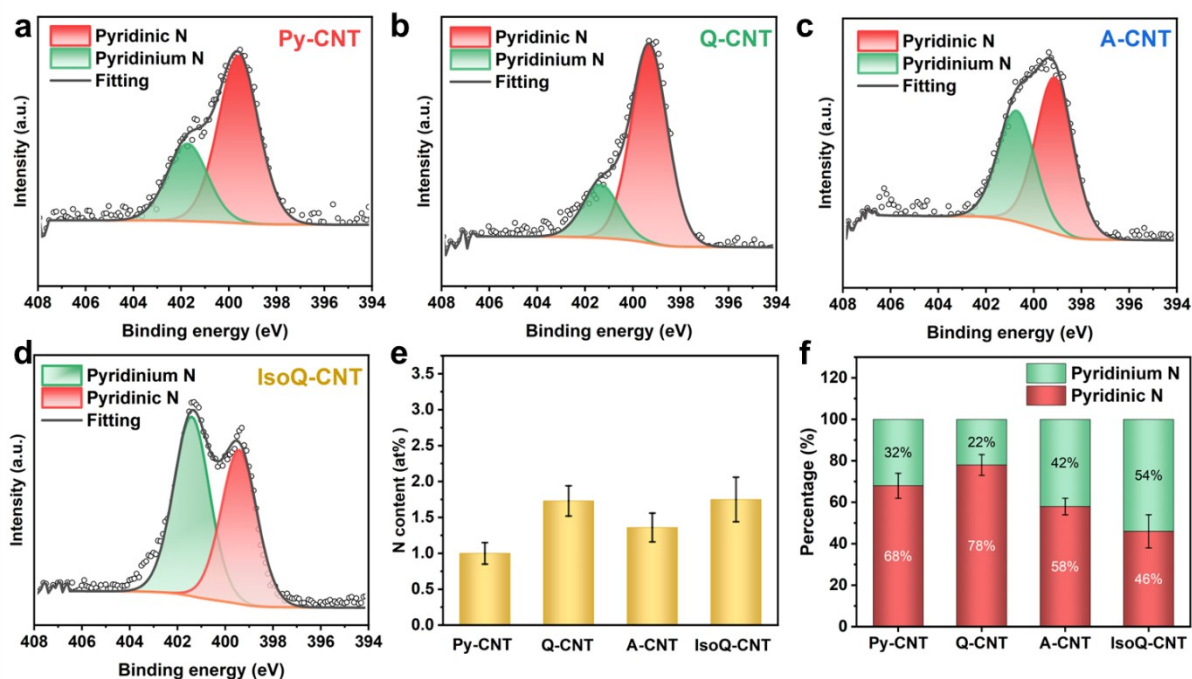$$L_a(nm) = 2.4 \times 10^{-10} \times \lambda^4{}_{nm}(\frac{I_G}{I_D}) \tag{4}$$

Figure S2 High-resolution N1s XPS spectra of Py-CNT (a); Q-CNT (b); A-CNT (c); and IsoQ-CNT (d). (e) the N content of different functionalized CNTs, and (f) the pyridinium N and pyridinic N ratio of different samples. The error comes from five individual points in one test.

Note2: N1s XPS spectra use a peak for pyridine species (N-C) at approximately 399 eV and full width at half maximum (FWHM) of 1.5 eV (red line) and a peak for pyridinium N species at approximately 401.2 eV and FWHM of 1.5 eV (green line). The peak in the pyrolyzed material observed between 401 eV and 402 eV is commonly associated with graphitic nitrogen (tertiary nitrogen structure). However, it is important to note that tertiary nitrogen cannot be synthesized during the reaction process, whereas pyridinium nitrogen (charged secondary nitrogen) can form and exhibit a similar binding energy. Therefore, we propose that this peak should be attributed to pyridinium nitrogen.

Table S2 Information of functionalized N-CNTs.

Entry	Material	I_D/I_G	La (nm)	N content (at%)	O content (at%)
1	CNT	0.30	128.4	0	2.31±0.62
2	Py-CNT	0.34	113.3	1± 0.15	2.48±0.43
3	Q-CNT	0.35	110.1	1.73±0.21	3.08±0.86
4	A-CNT	0.37	104.1	1.36±0.2	1.95±0.77
5	IsoQ-CNT	0.36	107.0	1.75±0.3	3.13±0.61
6	IsoQ-CNT2	-		2.96±0.3	2.12±0.55

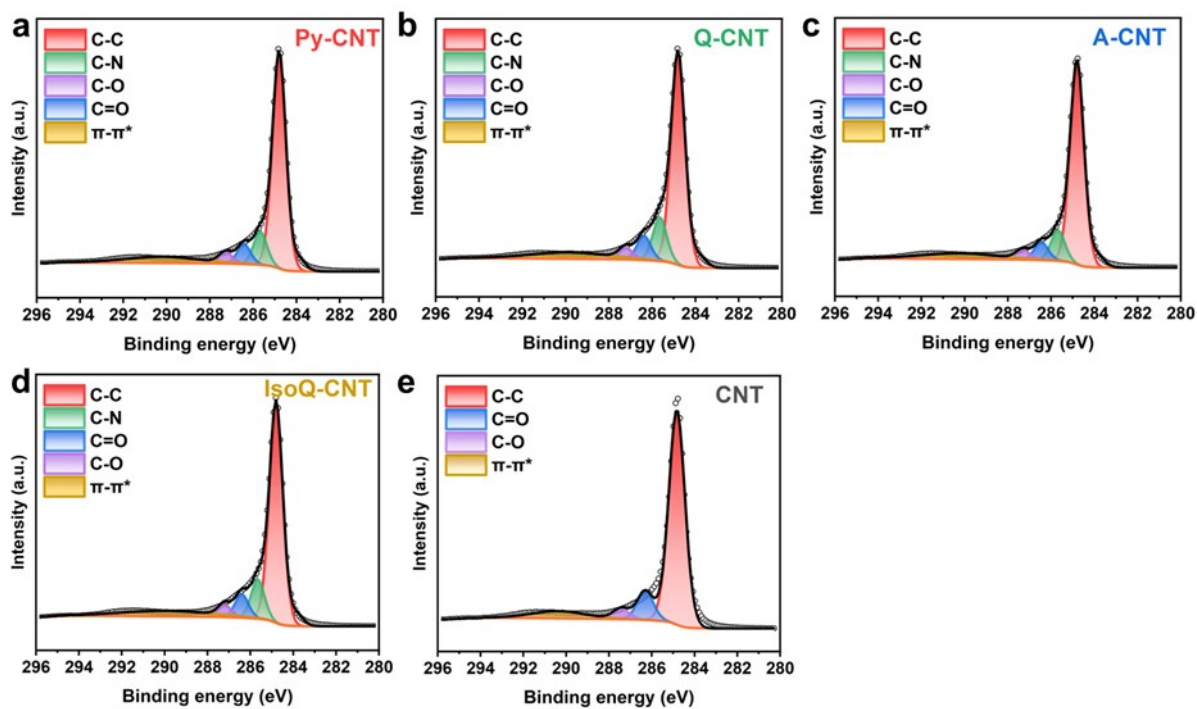The error of each sample is from 5 individual points of the XPS results.

Figure S3 High-resolution C1s XPS spectra of Py-CNT (a); Q-CNT (b); A-CNT (c); IsoQ-CNT (d); and CNT (e).
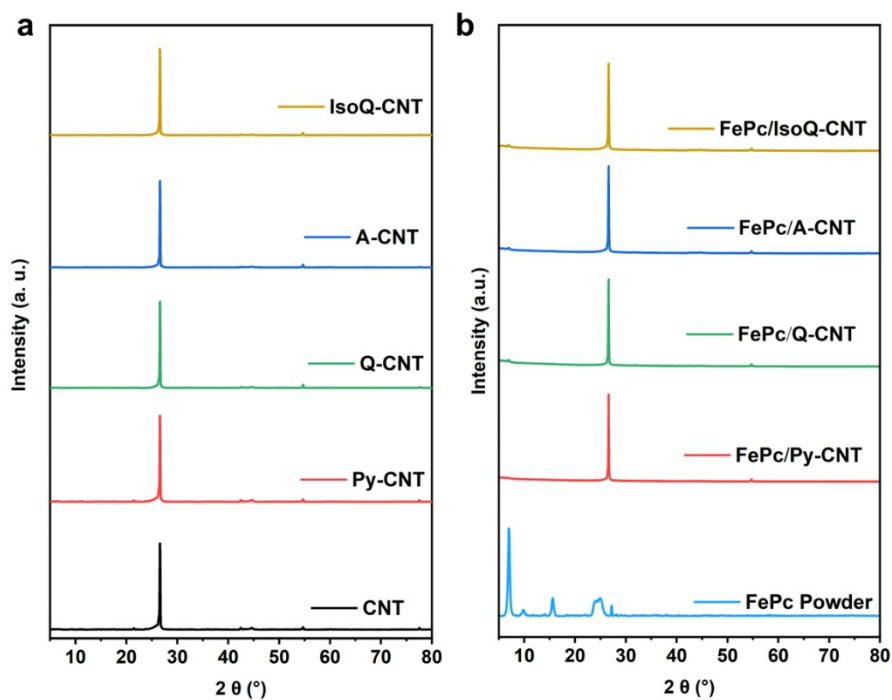
Figure S4 XRD pattern of (a) CNT, Py-CNT, Q-CNT, A-CNT, and IsoQ-CNT and (b) FePc powder, FePc/Py-CNT, FePc/Q-CNT, FePc/A-CNT, and FePc/IsoQ-CNT materials.
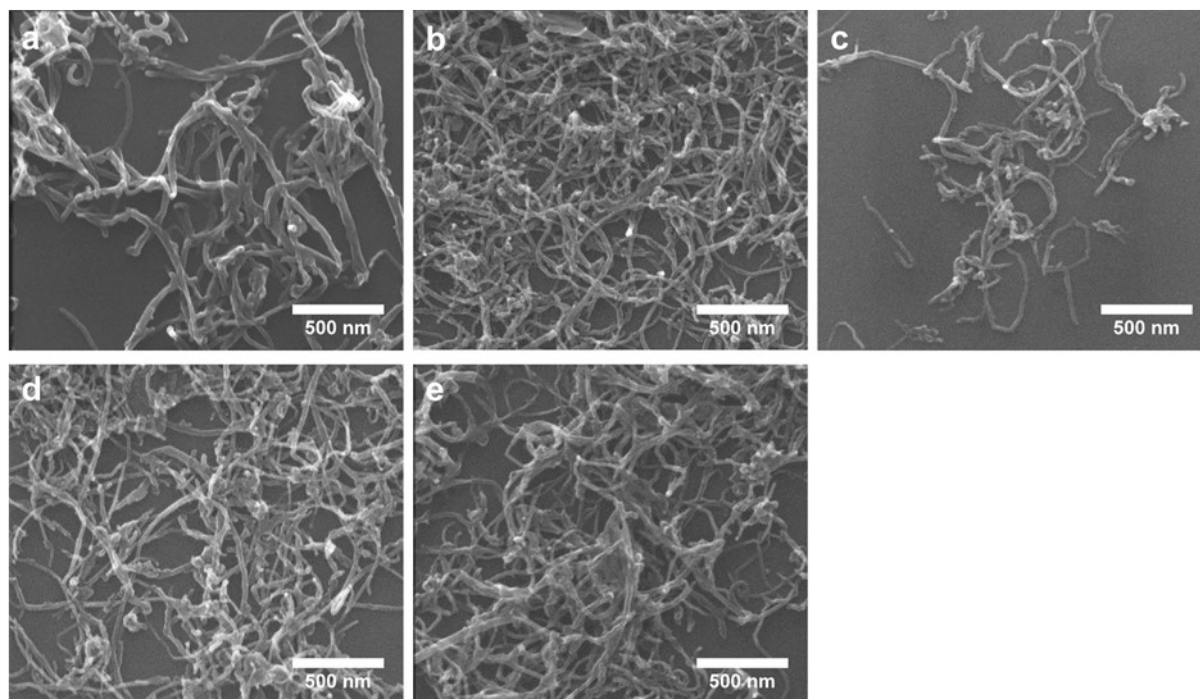

Figure 5 SEM images of CNT (a); FePc/Py-CNT (b); FePc/Q-CNT (c); FePc/A-CNT (d); FePc/IsoQ-CNT (e)
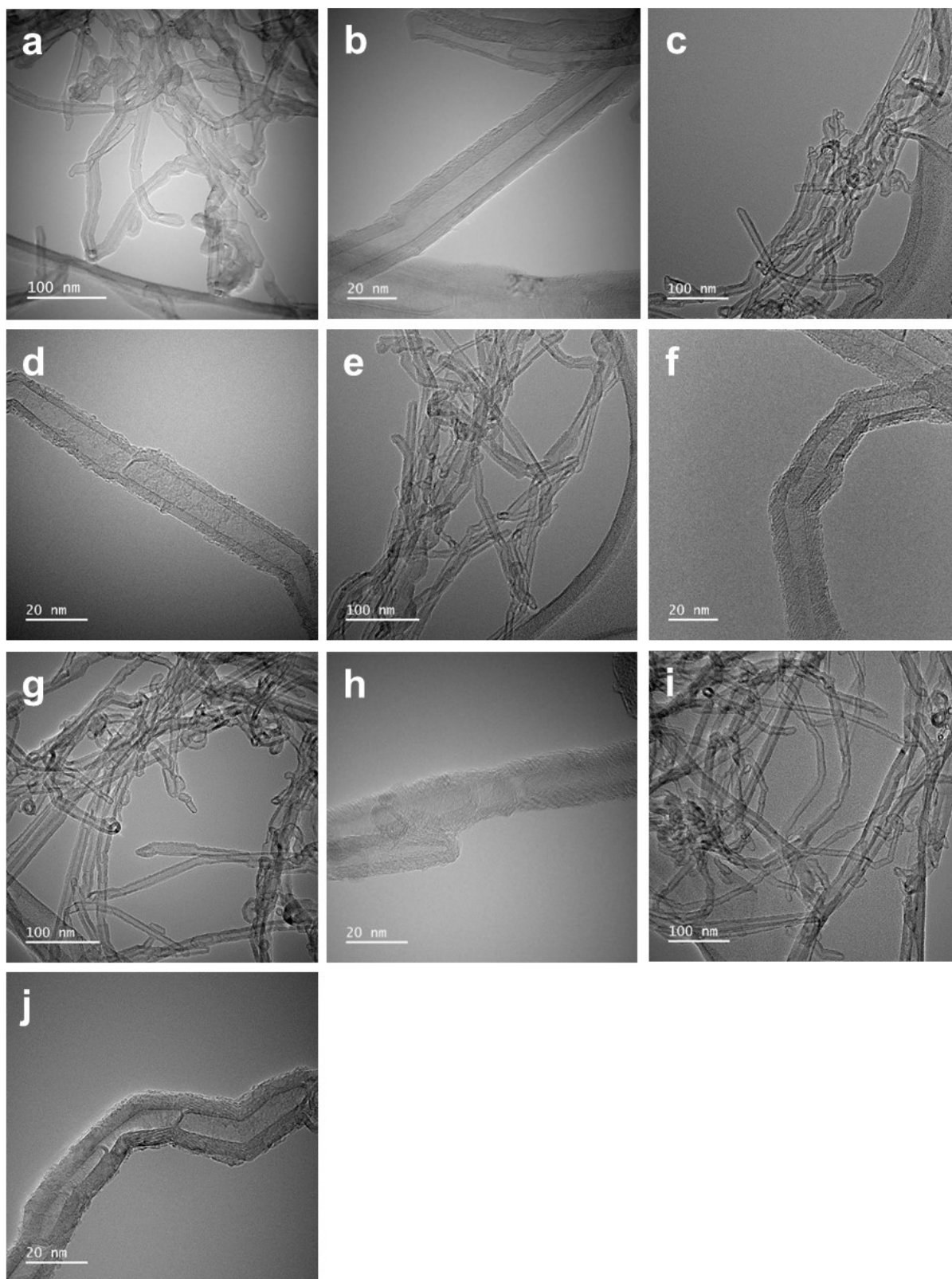
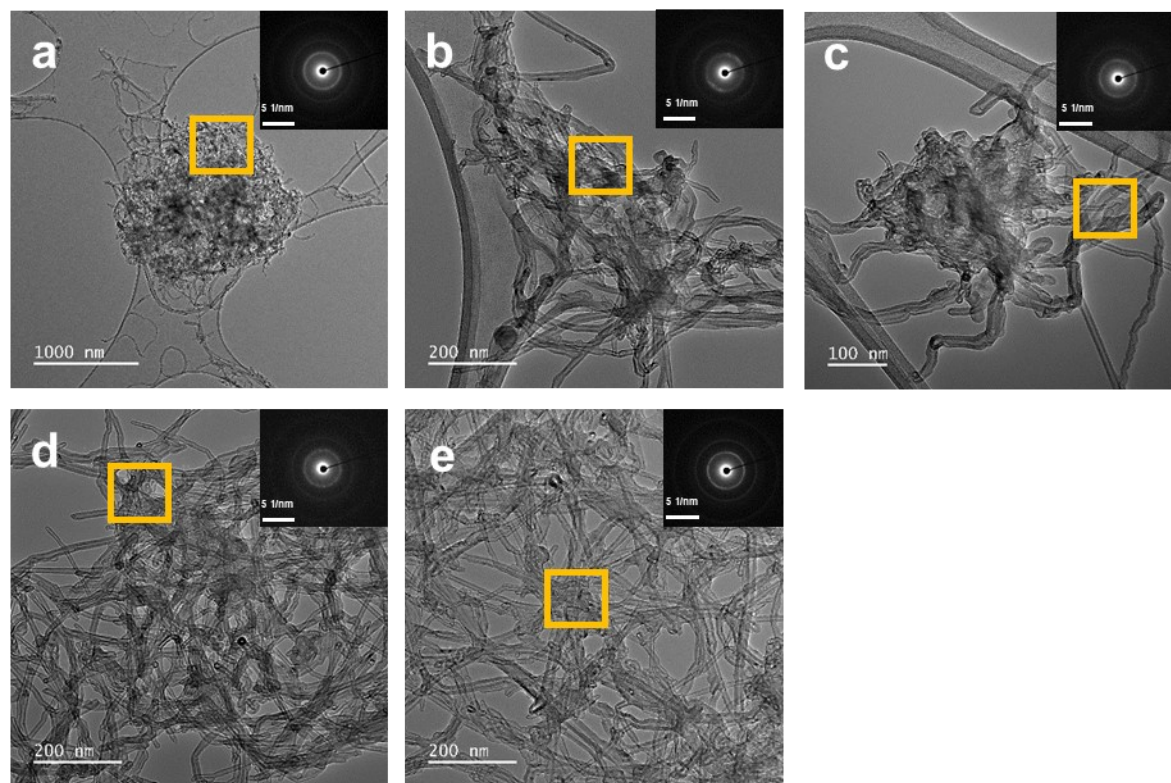Figure S6 TEM images of CNT (a) and (b); FePc/Py-CNT (c) and (d); FePc/Q-CNT (e) and (f); FePc/A-CNT (g) and (h); FePc/IsoQ-CNT(i) and (j).

Figure S7 TEM images and SAED of CNT(a); FePc/Py-CNT (b); FePc/Q-CNT (c); FePc/A-CNT (d); FePc/IsoQ-CNT (e).
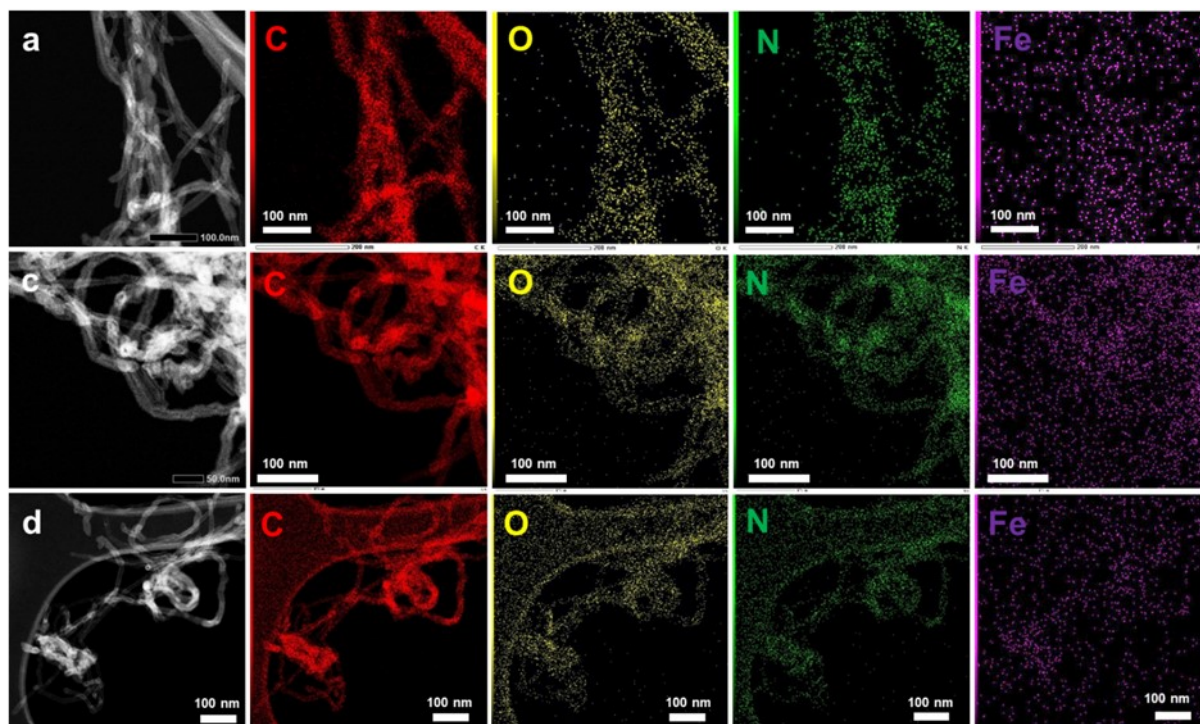

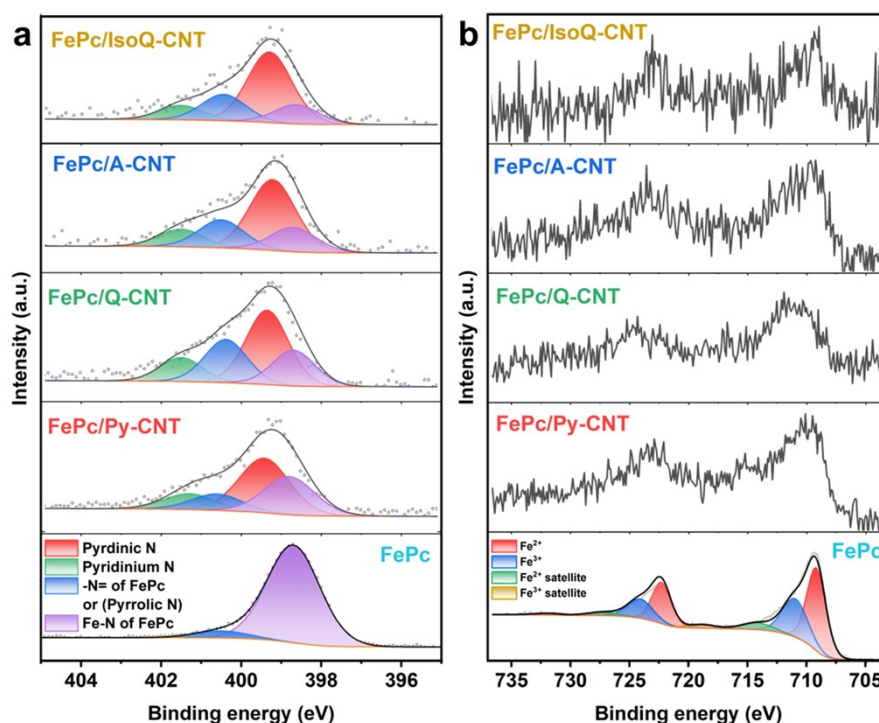Figure S8 HAADF-STEM and EDS mapping images of FePc/Q-CNT (a); FePc/A-CNT (b); and FePc/IsoQ-CNT(c).

Figure S9 (a) High-resolution N1s XPS spectra; (b) High-resolution Fe 2p XPS spectra of FePc, and FePc/N-CNTs.

Note 3: According to previous N-CNTs N1s XPS spectra fitting, the pyridine N peak is assigned at approximately 399 eV and FWHM ≈ 1.3 eV (red line), and the pyridinium N peak is assigned at approximately 401.2 eV and FWHM ≈ 1.3 eV (green line). The FePc powder N1s XPS spectra were fitted using a peak at approximately 398.7 eV and FWHM ≈ 1.4 eV (purple line, Fe-N of FePc), and a peak at approximately 400.5 eV and FWHM ≈ 1.4 eV (blue line, bridge N (-N=)). FWHM of deconvoluted peaks were set as equal in each spectrum.

Only the Fe 2p XPS spectrum of FePc powder was attempted to be fitted. The spectrum is composed of the Fe 2p doublet (2p3/2 and 2p1/2). The spin-orbit splitting was set to 13.1 eV and spin-orbit splitting signal intensities (areas) were set to 2:1 during the fitting. The 2p3/2 peak was fitted using a peak at 709.1 eV and FWHM ≈ 2.3 eV (red line, Fe^{2+}) and a peak at 711.0 eV and FWHM ≈ 2.3 eV (blue line, Fe^{3+}). Additionally, the Fe3+ satellite peak at 722.3 eV and FWHM ≈ 2.3 eV, and the Fe2+ satellite peak at 723.2 eV and FWHM ≈ 2.3 eV were used for the Fe 2p3/2 peak fitting.
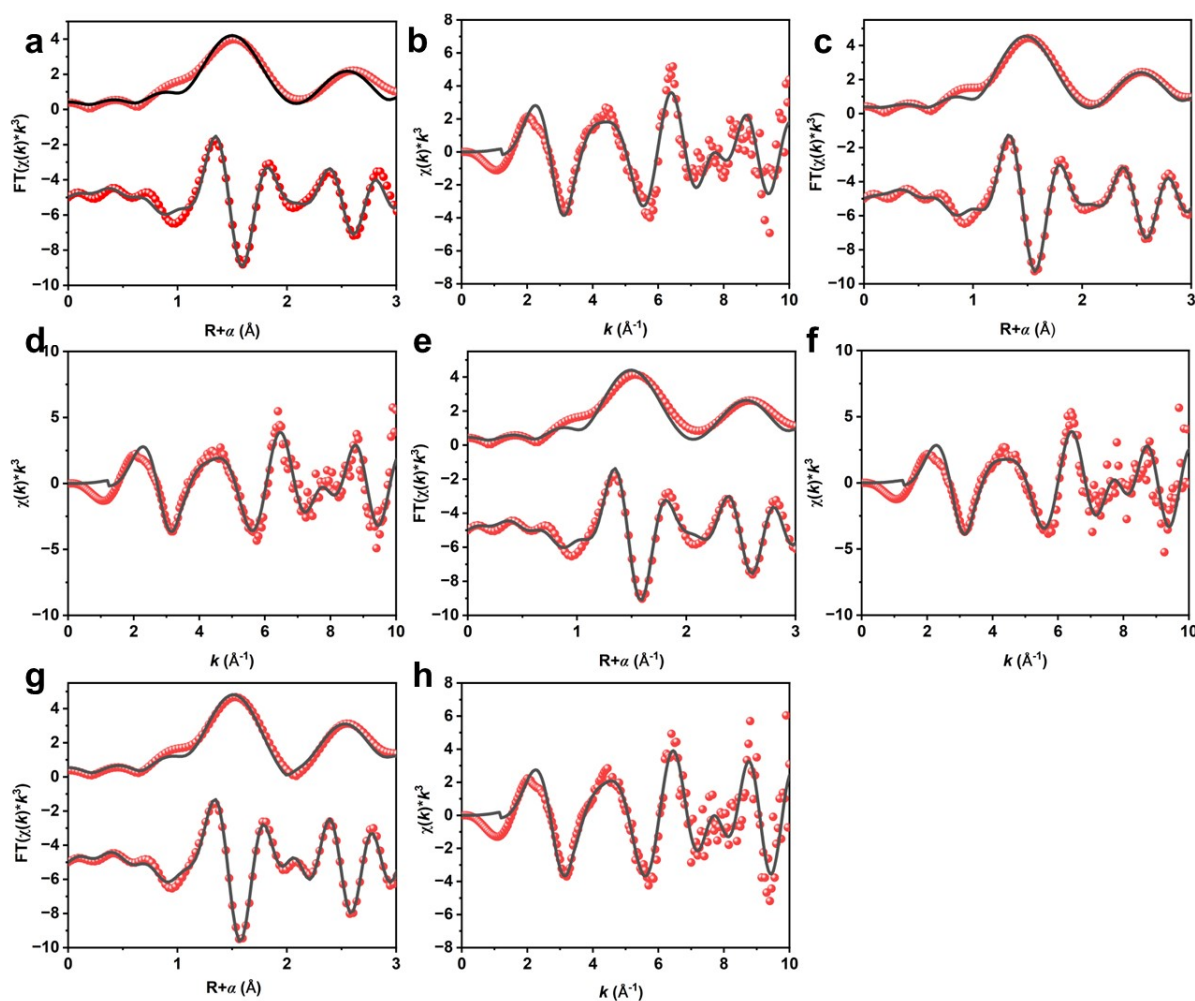
Figure S10 Fe K-edge EXAFS (points) and the curvefit (line) for FePc/Py-CNT (a), FePc/Q-CNT (c), FePc/A-CNT (e), FePc/IsoQ-CNT (g) shown in R-space (FT Magnitude and imaginary component) (The data are k3-weight and not phase-corrected); Fe K-edge EXAFS (points) and the curvefit (line) for FePc/Py-CNT (b), FePc/Q-CNT (d), FePc/A-CNT (f), FePc/IsoQ-CNT (h) and shown in K3 weighted K-space.

Table S3 EXAFS fitting parameters at the Fe K-edge for samples

Sample	Path	Coordination Number	R (Å)	σ2 (Å2)	△E0(eV)	R factor
FePc/Py-CNT	Fe-N	5.15±1.92	2.01±0.08	0.009±0.005	5.15±1.92	1.94%
	Fe-C	5.17±2.78	3.00±0.04	0.001±0.006		
FePc/Q-CNT	Fe-N	4.47 ± 1.12	1.99±0.07	0.006±0.003	6.18±2.32	1.60%
	Fe-C	4.74±1.71	2.99±0.03	0.001±0.004		
FePc/A-CNT	Fe-N	4.92±0.94	2.01±0.08	0.008±0.005	6.32±3.43	2.38%
	Fe-C	4.69±2.56	3.00±0.03	0.001±0.006		
FePc/IsoQ-CNT	Fe-N	5.10±1.96	1.98±0.06	0.008±0.002	5.05±1.70	0.78%
	Fe-C	4.30±1.12	2.98±0.02	0.002±0.003		
Fe foil	Fe-Fe1	8 (fixed)	2.45±0.01	0.006±0.002	2.01±1.90	1.4%
	Fe-Fe2	6 (fixed)	2.83±0.01	0.004±0.002		
	Fe-Fe3	12 (fixed)	4.04±0.02	0.009±0.002		

Note 4: R is the distance between absorber and backscatter atoms; σ^2 is the Debye-Waller factor to account for both thermal and structural disorders; $\triangle E_0$ is the inner potential correction and the R factor indicates the goodness of the fit. S0^2 (S0^2 = 0.8)is calculated by fitting the reference Fe foil with a fixed-CN path, and it is fixed when fitting for FePc/N-CNTs. The FePc/N-CNT samples were fitted with builted axially coordinated structural models. For Fe fitting, C. N. was fixed and S_0^2 was open, $\triangle E_0$ was refined as a global fit parameter, Data ranges: $3 \leq k \leq 12$ Å^{-1}, $1.0 \leq R \leq 4$ Å. The number of variable parameters is 8, out of a total of 16.9 independent data points. For FePc/N-CNTs fitting, S_0^2 is fixed as 0.8 according to the fitting of Fe foil, $\triangle E_0$ was refined as a global fit parameter. Data ranges: $3 \leq k \leq 10$ Å^{-1}, $1.0 \leq R \leq 3$ Å. The number of variable parameters is 7, out of a total of 8 independent data points.

Table S4 S4 Fe content of FePc/N-CNT.

	FePc/Py-CNT	FePc/Q-CNT	FePc/A-CNT	FePc/IsoQ-CNT	FePc/IsoQ-CNT2
XPS Fe (at%)	0.52±0.02	0.33±0.15	0.54±0.08	0.35±0.02	0.51±0.03
ICP Fe (wt%)	0.22+0.01	0.23+0.01	0.32	0.33+0.08	0.35+0.01

The ICP-MS tests for each sample were repeated two times and the XPS content was calculated based on 5 different points for each sample.
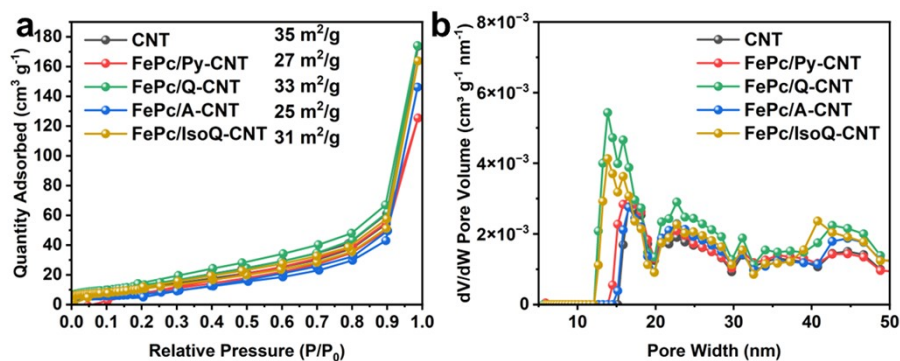

Figure S11(a) N2 adsorption and desorption isotherms with specific BET surface areas and (b) pore distribution of pristine and FePc/N-CNTs.
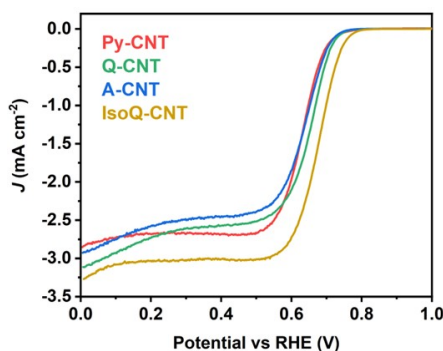
Figure S12 Cathodic LSV curves obtained by subtracting N_2-saturated LSV from the O_2-saturated result (in 0.1 M KOH with a rotation rate of 1600 rpm recorded at 10 mV s^{-1}).

Table S5 Electrochemical results for FePc/N-CNT.

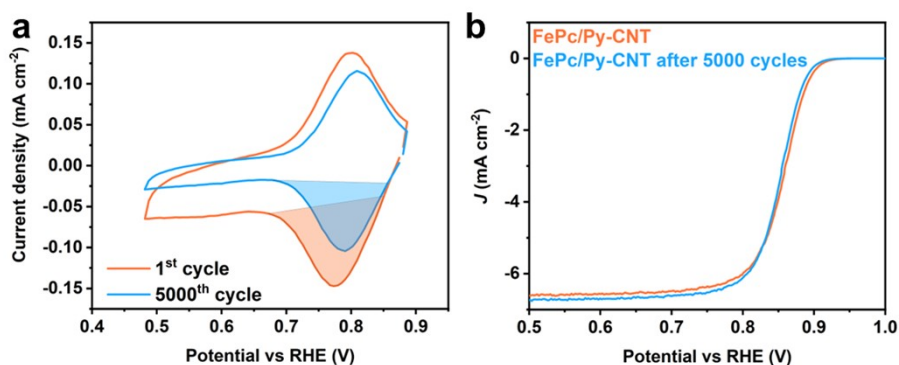|	FePc/Py-CNT	FePc/Q-CNT	FePc/A-CNT	FePc/IsoQ-CNT
Fe^{2+}/Fe^{3+}redox potential (V_{RHE})	0.80	0.76	0.79	0.78
Potential (V_{RHE}) @ 0.1 mA cm^{-2}	0.91±0.003	0.89±0.002	0.91±0.002	0.90±0.003
m_{kin}@0.85V_{RHE}	21.2±0.66	8.0±1.37	12.6±0.81	20.1±1.03
SD_{CV}(site cm^{-2})	1.95×10^{18}	2.39×10^{18}	2.21×10^{18}	2.06×10^{18}
TOF_{CV} @0.85V_{RHE} (e$^-$ site^{-1} s^{-1})	19.0±0.60	5.9±1.00	10.0±0.64	17.1±0.87
TOF_{ICP} @0.85V_{RHE} (e$^-$ site^{-1} s^{-1})	5.6±0.18	2.0±0.34	2.3±0.15	3.5±0.18

Figure S13 (a) CV curves in N_2-saturated 0.1 M KOH with a rotation rate of 0 rpm at 100 mV s^{-1} scan rate from 0.5 V_{RHE} to 0.9 V_{RHE}. The scan shown here is the first and 5000th collected; (b) O_2 saturated cathodic LSV curves obtained before (orange line) and after (blue line) 5000 CV scans (in N_2 saturated 0.1 M KOH with a rotation rate of 1600 rpm recorded at 10 mV s^{-1}). The capacitance correction is applied by subtracting equivalent measurements in N_2.

Note 5: RDE-based accelerated stress test was conducted over 5000 cycles between 0.9–0.5 V_{RHE} at 100 mV s^{-1} under N_2 saturation. After the cycling, we did not observe any catalyst powder coming off the electrode, while the color of the electrolyte became slightly yellow, indicating the degradation may come from the dissolution of Fe. The kinetic current density falls from 11.50 mA cm^{-2} to 10.04 mA cm^{-2} at 0.85 V_{RHE}, equivalent to a 12.7 % reduction. The electrochemically active Fe sites of the catalyst could be calculated based on the $Fe^{2+/Fe3+}$ peak integration in CV via Equation 2. As a result, The integrated area of this $Fe^{2+/Fe3+}$ reduction peak could be utilized to estimate the electrochemical active Fe site density. The integrated results of the CV 1st and 5000th suggest approximately 25% of redox-active Fe was lost during the process.
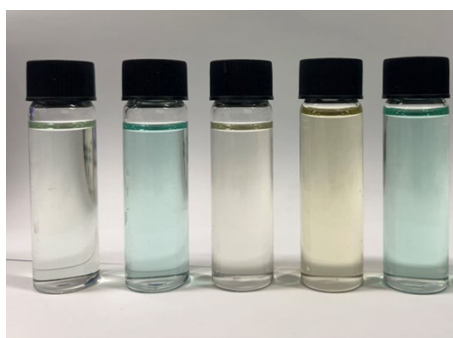

Figure S14 The photograph of FePc in DMF solutions: from left to right pristine FePc, FePc + pyridine, FePc + quinoline, FePc + acridine, FePc + isoquinoline.

Note 6: The FePc DMF solution of a certain concentration (1mg/ 20 ml 0.088M) was prepared, and then 10 equivalents of these four pyridine derivatives (pyridine, quinoline, acridine, and isoquinoline) were added respectively. 10 times molar ratio of small molecules is chosen to ensure the FePc could be easily axially coordinated quickly. It is interesting to find that these four different mixed solutions changed after 5 minutes of sonication. The color of solutions with pyridine and isoquinoline becomes bright blue, while there is no obvious color change in the solution with quinoline and acridine. Considering quinoline, acridine, and isoquinoline are not colorless chemicals, UV-vis tests were performed for these four mixture solutions.
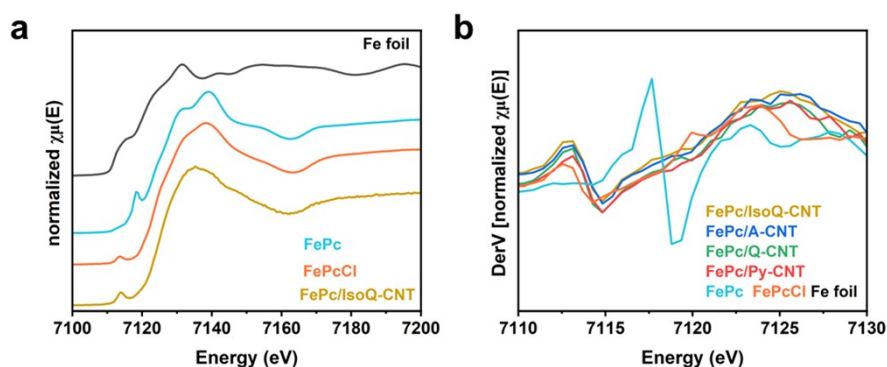
Figure S15(a) Fe K-edge XANES spectra of as-prepared FePc/IsoQ-CNTs in comparison with Fe foil, Fe(II)Pc, and Fe(III)PcCl (b) normalized first-derivative spectra of as-prepared FePc/N-CNTs in comparison with Fe foil, Fe(II)Pc, and Fe(III)PcCl
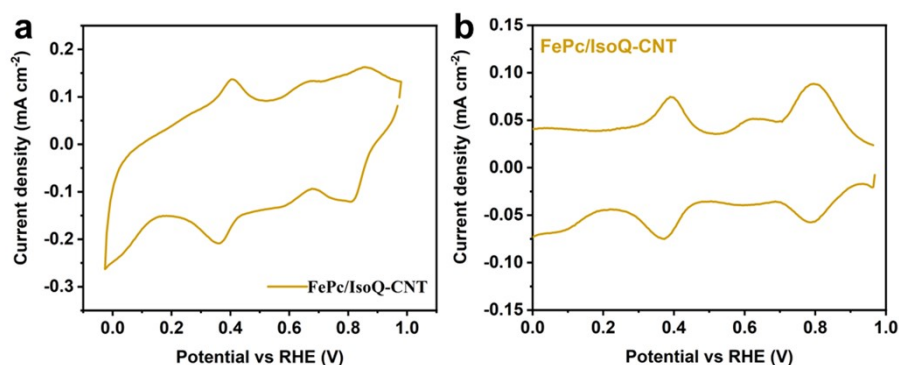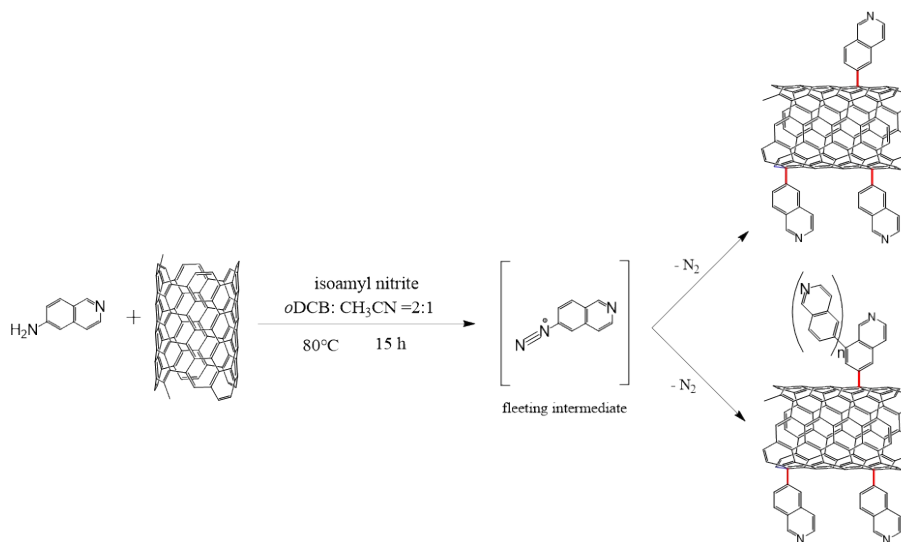

Figure S16 (a) CV of FePc/IsoQ-CNT in N_2-saturated 0.1 M KOH, in static conditions with a scan rate of 100 mV/s. (b) SWV was obtained in N_2-saturated, in static conditions, with a frequency of 2 Hz, with 4 mV steps, and a modulation amplitude of 20 mV.

Scheme S1 Aryl diazonium reaction to functionalize CNT surfaces and aryl-aryl coupling as a possible side reaction

Note 7: The aryl diazonium reaction is a type of radical reaction where diazonium cations are reduced, accompanied by electron transfer and the loss of dinitrogen, leading to the formation of aryl radicals. Besides forming C-C bonds with carbon surfaces, it is also possible for polymers (multilayers) to form through azo or aryl coupling reactions with highly active aryl radicals.[13, 14] However, azo coupling reactions typically occur under mildly acidic conditions and at low temperatures (0-10°C) due to the instability of azo dyes. A previous study has indicated that the main reaction occurring with CNTs is aryl coupling.[15] In this scheme, we present one possible multilayer structure by aryl coupling, though the exact coupling position requires further investigation.

As shown in Table S1 and Table S2, although the stoichiometric ratio of CNTs to the four different precursors was kept constant, it was observed that amino-isoquinoline led to functionalized CNTs with a higher nitrogen content, potentially exhibiting higher relative functionalization efficiency. However, it is notable that extensive polymerization of aryl groups has been observed during electrochemical aryl diazonium reactions in previous reports.[16-18] As such, the possibility of the reaction occasionally occurring on molecules already attached to CNTs, rather than proceeding exclusively on the CNT surface cannot be excluded. This would result in the formation of short organic chains on the surface of the CNT and should be considered in cases, especially the isoQ-CNTs sample that exhibited higher nitrogen content.
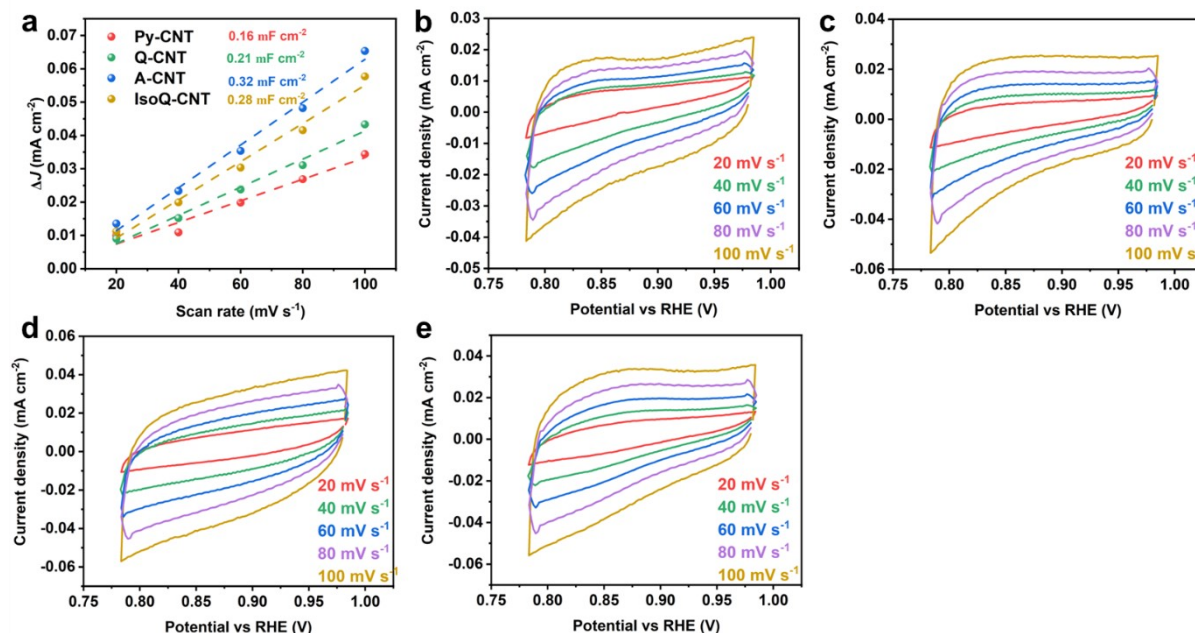

Figure S17 (a) the current densities ($\Delta j = J_{anode} - J_{cathode}$, at 0.9 V_{RHE}) as a function of scanning rates with the corresponding slope being twice that of the C_{dl} values. CV from 0.78 V_{RHE} to 0.97 V_{RHE} of Py-CNT (b), Q-CNT(c), A-CNT(d), and IsoQ-CNT (e) recorded at 20, 40, 60, 80, 100 mV s^{-1} in N^2-saturated 0.1 M KOH at 0 rpm.
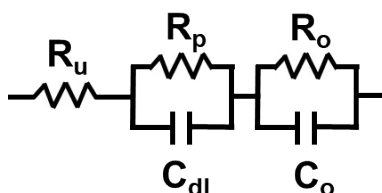

Figure S18 (a) Equivalent circuit for fitting of Impedance spectroscopy measurements

Note 8: In the equivalent circuit we used here, at higher frequencies, the circuit consists of polarization resistance (Rp), double-layer capacitance (C$_{dl}$), and uncompensated resistance (Ru). The uncompensated resistance, also known as the ohmic drop, reflects the electrolyte's ohmic resistance between the reference and working electrodes. The polarization resistance primarily encompasses the charge transfer resistance. At lower frequencies, the presence of a semicircle is typically associated with oxygen transport. This can be represented by a simple resistance (Ro). Co represents the capacitance arising from the diffusion process. Instead of employing pure capacitance elements, we choose constant phase elements for fitting.

Table S6 Results of the fitting obtained with the equivalent circuits

	R_p	C_{dl} (nF)	R_o	C_o (mF)
FePc/Py-CNT	30.29	330	25.08	8.20
FePc/Q-CNT	40.19	174	64.24	6.51
FePc/A-CNT	40.84	310	31.58	8.66
FePc/IsoQ-CNT	35.99	191	40.95	7.05
FePc/IsoQ-CNT2	41.42	145	46.39	6.93
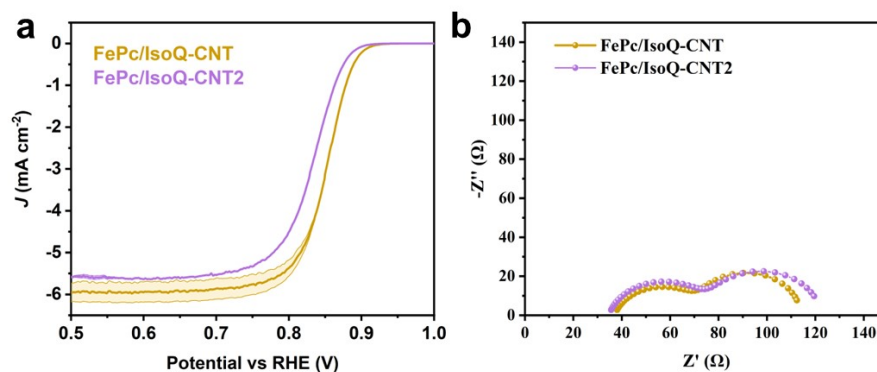
Figure S19 (a) Cathodic LSV curves obtained by subtracting N_2-saturated LSV from the O_2-saturated result (in 0.1 M KOH with a rotation rate of 1600 rpm recorded at 10 mV s^{-1}); (b) Electrochemical impedance spectroscopy of FePc/IsoQ-CNT and FePc/IsoQ-CNT2. Data were collected at 0.85 V_{RHE} in a frequency range of 0.1 Hz to 1 M Hz, in oxygen-saturated 0.1 M KOH at a rotational rate of 1600 rpm.
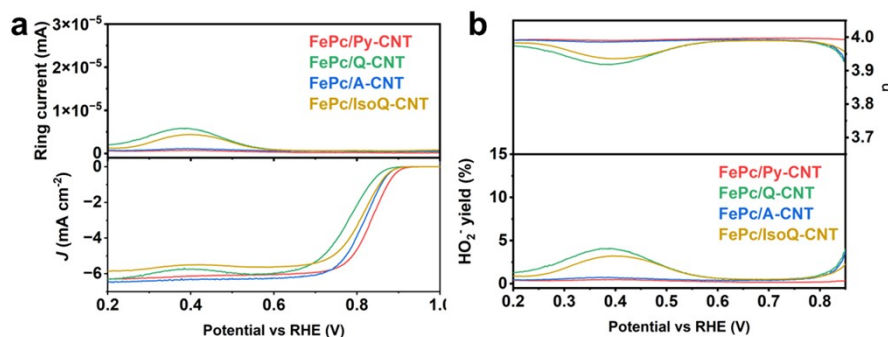

Figure S20 (a) Cathodic scan RRDE measurement in O_2 saturated 0.1 m KOH at 1600 rpm, 10 mV s^{-1}. (b) H_2O_2 production and electron transfer numbers were calculated.
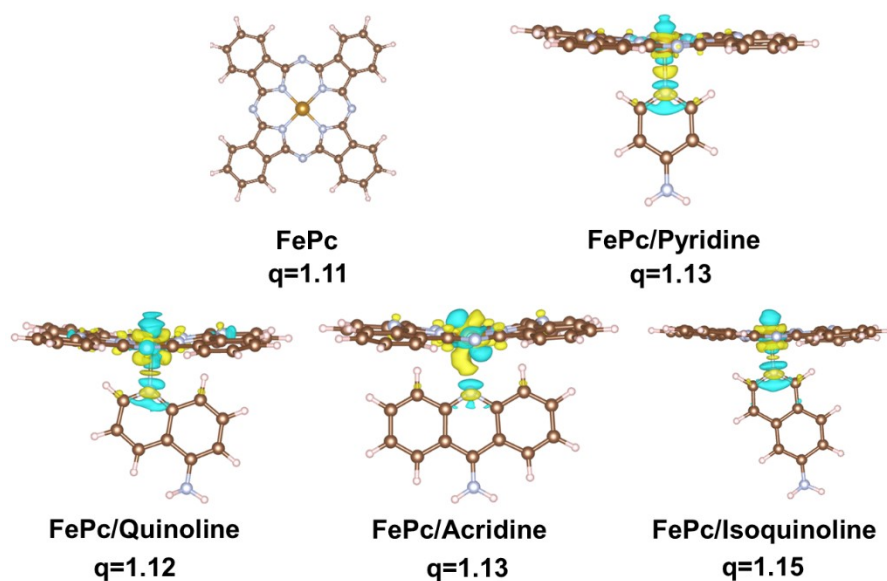
Figure S21 Charge-density difference of FePc, Pyridine-FePc, Quinoline-FePc, Acridine-FePc, and isoquinoline-FePc
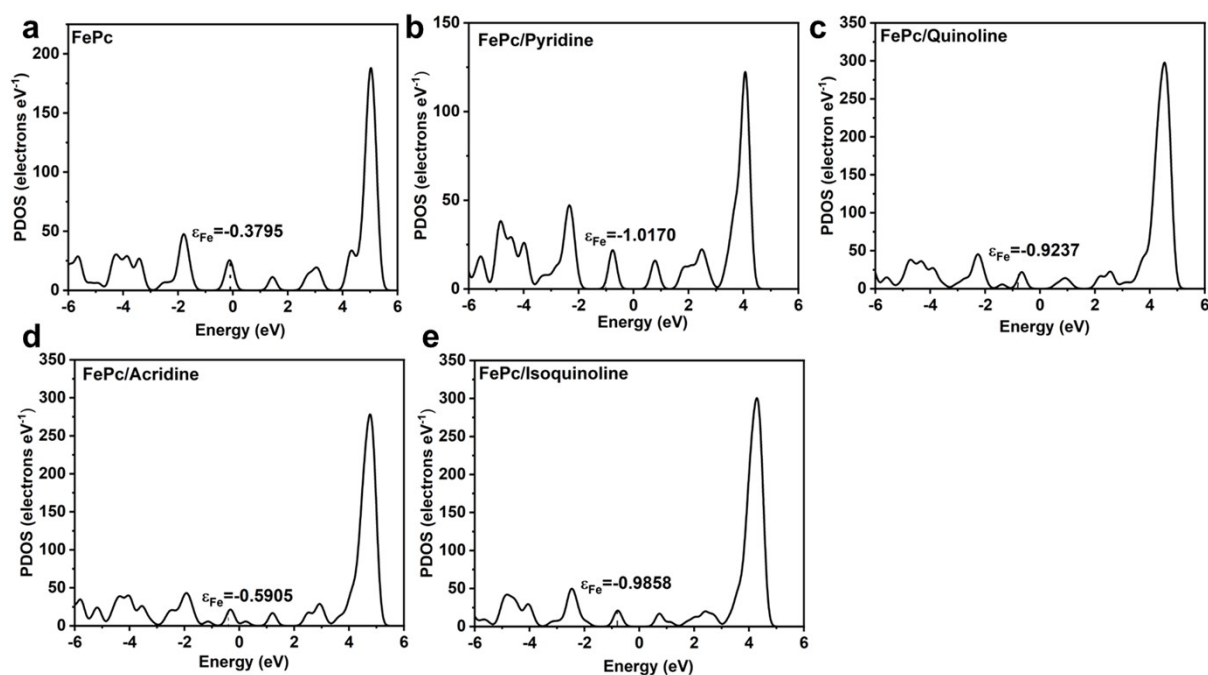

Figure S22 PDOS curves of (a) FePc; (b) Pyridine-FePc; (c) Quinoline-FePc; (d) Acridine-FePc; and (e) isoquinoline-FePc
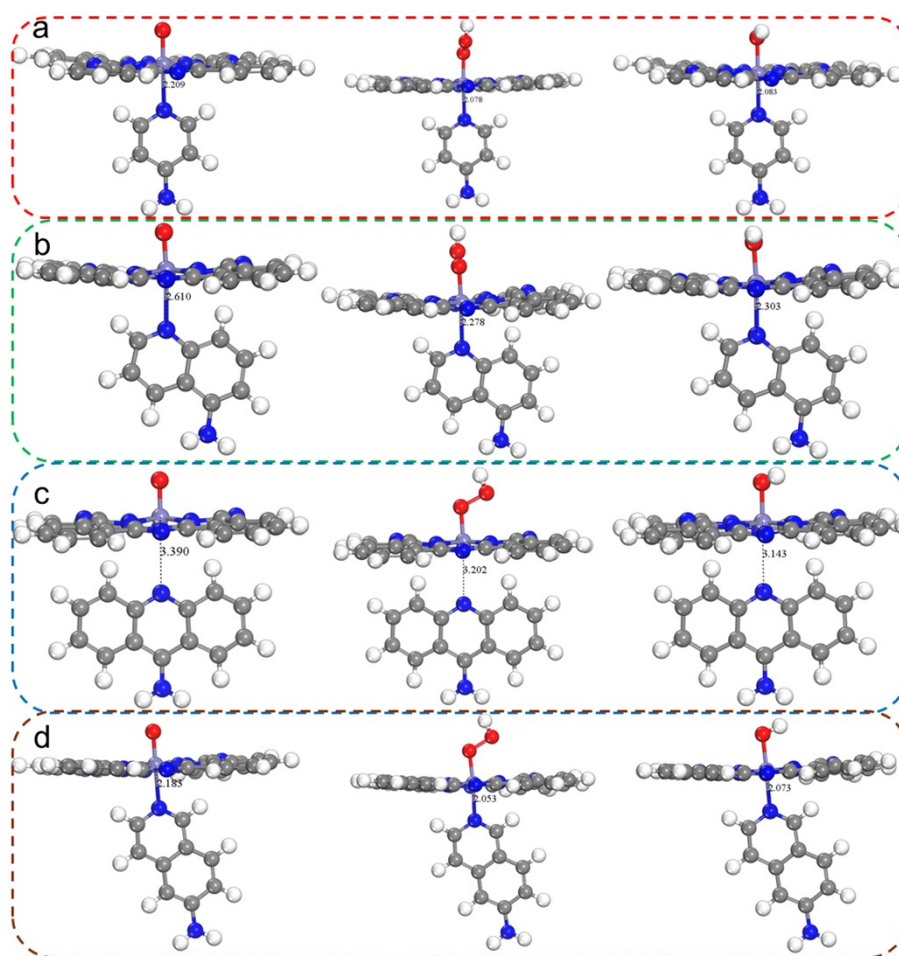
Figure S23 Views of structure of (a), FePc/Py with *O_2, *OOH, and *OH, (b) FePc/Q with *O_2, *OOH, and *OH, (c) FePc/Q with *O_2, *OOH, and *OH, (d) FePc/isoQ with *O_2, *OOH and *OH intermediates. The length of the axial coordination Fe-N bond was figured out in each figure.
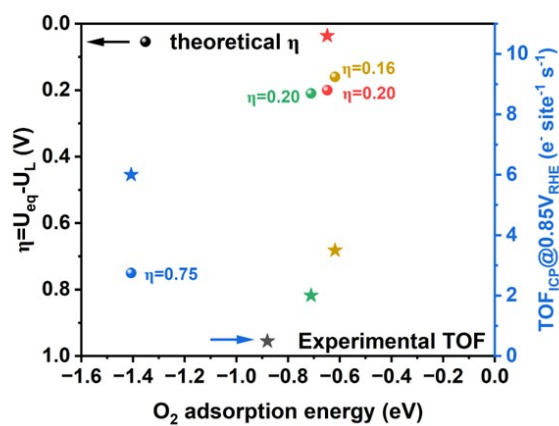

Figure S24 The theoretical ORR overpotential on FePc/N-heterocycles in vacuum and experimental TOF on FePc/N-CNT catalysts versus their O2 adsorption energy. FePc/Py (red), FePc/Q (green), FePc/A (blue), and FePc/IsoQ (yellow).

Reference

1. B. Ravel and M. Newville, *Journal of Synchrotron Radiation*, 2005, **12**, 537-541.
2. A. Tenderholt, B. Hedman, K. O. Hodgson and S. Stanford Synchrotron Radiation Laboratory, Stanford University, Menlo Park CA 94025], *AIP Conference Proceedings*, 2007, **882**, Medium: X; Size: page(s) 105-107 2010-2006-2003.
3. J. J. Rehr, J. J. Kas, M. P. Prange, A. P. Sorini, Y. Takimoto and F. Vila, *Comptes Rendus. Physique*, 2009, **10**, 548-559.
4. G. Kresse and J. Furthmüller, *Computational Materials Science*, 1996, **6**, 15-50.
5. J. P. Perdew, K. Burke and M. Ernzerhof, *Physical Review Letters*, 1996, **77**, 3865-3868.
6. S. Grimme, J. Antony, S. Ehrlich and H. Krieg, *The Journal of Chemical Physics*, 2010, **132**.
7. V. Wang, N. Xu, J.-C. Liu, G. Tang and W.-T. Geng, *Computer Physics Communications*, 2021, **267**, 108033.
8. J. K. Nørskov, J. Rossmeisl, A. Logadottir, L. Lindqvist, J. R. Kitchin, T. Bligaard and H. Jonsson, *J The Journal of Physical Chemistry B*, 2004, **108**, 17886-17892.
9. H. Fei, J. Dong, Y. Feng, C. S. Allen, C. Wan, B. Volosskiy, M. Li, Z. Zhao, Y. Wang, H. Sun, P. An, W. Chen, Z. Guo, C. Lee, D. Chen, I. Shakir, M. Liu, T. Hu, Y. Li, A. I. Kirkland, X. Duan and Y. Huang, *Nature Catalysis*, 2018, **1**, 63-72.
10. L. Cheng, C. Ma, W. Lu, X. Wang, H. Yue, D. Zhang and Z. Xing, *Chemical Engineering Journal*, 2022, **433**.
11. W. Li, D. Peng, W. Huang, X. Zhang, Z. Hou, W. Zhang, B. Lin and Z. Xing, *Carbon*, 2023, **204**, 315-324.
12. J. Ribeiro-Soares, M. E. Oliveros, C. Garin, M. V. David, L. G. P. Martins, C. A. Almeida, E. H. Martins-Ferreira, K. Takai, T. Enoki, R. Magalhães-Paniago, A. Malachias, A. Jorio, B. S. Archanjo, C. A. Achete and L. G. Cançado, *Carbon*, 2015, **95**, 646-652.
13. B. D. Assresahegn, T. Brousse and D. Bélanger, *Carbon*, 2015, **92**, 362-381.
14. P. Doppelt, G. Hallais, J. Pinson, F. Podvorica and S. Verneyre, *Chemistry of Materials*, 2007, **19**, 4570-4575.
15. J. M. Tour, C. A. Dyke, M. P. Stewart and F. Maya, *Synlett*, 2004, **1**, 155-160.
16. S. Phal, K. Shimizu, D. Mwanza, P. Mashazi, A. Shchukarev and S. Tesfalidet, *Molecules*, 2020, **25**.
17. C. Saby, B. Ortiz, G. Y. Champagne and D. Bélanger, *Langmuir*, 1997, **13**, 6805-6813.
18. J. K. Kariuki and M. T. McDermott, *Langmuir*, 2001, **17**, 5947-5951.